POLITECNICO DI TORINO
Repository ISTITUZIONALE

Modelling the non-linear viscoelastic behaviour of brain tissue in torsion

Original
Modelling the non-linear viscoelastic behaviour of brain tissue in torsion / Small, G., Ballatore, F., Giverso, C., Balbi, V.. - In: SOFT MATTER. - ISSN 1744-683X. - 21:26(2025), pp. 5268-5283. [10.1039/d5sm00138b]

Availability:
This version is available at: 11583/3004659 since: 2025-10-30T16:42:09Z

Publisher:
Royal Society of Chemistry - RSC

Published
DOI:10.1039/d5sm00138b

Terms of use:

This article is made available under terms and conditions as specified in the corresponding bibliographic description in the repository

Publisher copyright

(Article begins on next page)

26 November 2026

Soft Matter

PAPER

View Article Online
View Journal

Check for updates

Cite this: DOI: 10.1039/d5sm00138b

Modelling the non-linear viscoelastic behaviour of brain tissue in torsion†

Griffen Small, *[a] Francesca Ballatore, [b] Chiara Giverso [b] and Valentina Balbi[a]

Brain tissue accommodates non-linear deformations and exhibits time-dependent mechanical behaviour. The latter is one of the most pronounced features of brain tissue, manifesting itself primarily through viscoelastic effects such as stress relaxation. To investigate its viscoelastic behaviour, we performed ramp-and-hold relaxation tests in torsion on freshly slaughtered cylindrical ovine brain samples (25 mm diameter and ∼10 mm height). The tests were conducted using a commercial rheometer at varying twist rates of {40, 240, 400} rad m^{-1} s^{-1}, with the twist remaining fixed at ∼88 rad m^{-1}, which generated two independent datasets for torque and normal force. The complete set of viscoelastic material parameters was estimated *via* a simultaneous fit to the analytical expressions for the torque and normal force predicted by the modified quasi-linear viscoelastic model. The model's predictions were further validated through finite element simulations in FEniCS. Our results show that the modified quasi-linear viscoelastic model—recently reappraised and largely unexploited—accurately fits the experimental data. Moreover, the estimated material parameters are in line with those obtained in previous studies on brain samples under torsion. These material parameters could enhance our understanding of slow-progressing pathologies such as tumour growth or neurodegeneration and inform the development of improved *in silico* models for brain surgery planning and training. Our novel testing protocol also offers an efficient, robust and reliable method for determining the viscoelastic properties of brain tissue under much more rapid loading conditions, which are of crucial importance for modelling traumatic brain injury.

Received 7th February 2025,
Accepted 19th May 2025

DOI: 10.1039/d5sm00138b

rsc.li/soft-matter-journal

Open Access Article. Published on 23 May 2025. Downloaded on 6/19/2025 2:26:22 PM.
This article is licensed under a Creative Commons Attribution 3.0 Unported Licence.

1 Introduction

Among all the tissues in the human body, brain tissue is the softest, with a shear modulus of the order of one kilopascal.[1] It is also, arguably, the most important, intricate and least understood. As is the case for most biological soft tissues, brain tissue displays highly complex mechanical behaviour: it can accommodate finite deformations and its response to applied forces is markedly non-linear;[2,3] it is incompressible and biphasic, consisting of a porous solid matrix saturated with an interstitial fluid;[1,4] it is structurally anisotropic[1] and it exhibits isotropic, time-dependent mechanical behaviour.[5–7] The latter is one of the most pronounced features of brain tissue, manifesting itself primarily through so-called viscoelastic effects. For instance, when brain tissue is deformed rapidly and then held in position, the corresponding stress decreases with time,[8] known as stress relaxation. Conversely, when a load is quickly applied and then maintained, the resulting strain increases over time,[9] known as creep. This behaviour is commonly observed in many biological tissues and can be attributed to either viscoelastic or plastic effects.[10–12] Other time-dependent mechanical effects exhibited by brain tissue include hysteresis and softening resulting from cyclic loading and unloading.[8]

The remarkable growth in computational power and technology since the turn of the millennium has led to increased demand from the clinical and biomedical communities for robust, accurate and efficient *in silico* mechanical models that can capture the behaviour of brain tissue in complex real-world scenarios, such as predicting disease progression,[1] surgical planning and training[13] and estimating injury risk for contact[14] and equestrian sports.[15] The wide range of applications above highlights one of the significant challenges facing the computational mechanics community: realistic predictions of brain tissue's mechanical response require sophisticated constitutive models that capture as much of the underlying physics as possible, yet these models must be simple and tractable enough to enable rapid and reliable estimation of their material parameters through calibration with experimental data.

Viscoelasticity is a major and active area of interest within the field of soft tissue mechanics. For a comprehensive overview of the subject and review of the classical models, the

[a] School of Mathematical and Statistical Sciences, University of Galway, College Road, Galway, Ireland. E-mail: g.small1@universityofgalway.ie
[b] Department of Mathematical Sciences "G. L. Lagrange", Politecnico di Torino, Corso Duca degli Abruzzi 24, Turin, Italy

† Electronic supplementary information (ESI) available. See DOI: https://doi.org/10.1039/D5SM00138B

Open Access Article. Published on 23 May 2025. Downloaded on 6/19/2025 2:26:22 PM. This article is licensed under a Creative Commons Attribution 3.0 Unported Licence.

reader is directed to the detailed articles.[16,17] The most straightforward constitutive theory that can be used to predict the viscoelastic behaviour of brain tissue is linear viscoelasticity, where the instantaneous stress is determined by convolving the strain history with a time-dependent function that depends on brain tissue's material properties.[18,19] In reality, brain tissue's viscoelastic response is markedly non-linear and its stress relaxation curves depend on the strain level. A non-linear viscoelastic constitutive theory is, therefore, essential for accurate predictions. Although the literature is replete with non-linear models,[16,17] they are generally difficult to employ in real-world biomechanical scenarios and numerically costly *vis-à-vis* model fitting and material parameter estimation. To this end, Fung, in his seminal work,[20] proposed a compromise approach now known as quasi-linear viscoelasticity (QLV). The QLV model, which falls under the umbrella of the more general Pipkin–Rogers model,[16] is the simplest extension of the linear viscoelastic theory to finite deformations. In contrast to the Pipkin–Rogers model, QLV is limited to materials whose viscous relaxation rates are independent of the instantaneous local strain[21] and thereby cannot account for the non-linear phenomenon of strain-dependent relaxation commonly observed in biological soft tissues.[22–25] Nevertheless, its relative simplicity compared to more general non-linear viscoelastic models has led to its widespread use. The QLV model has been employed to model a myriad of biological soft tissues including the skin,[26,27] liver,[28] brain,[5–7,29–34] lung,[35] eye,[36] spinal cord,[37–39] prostate gland,[40] eardrum,[41] oesophagal tissue,[42] heart muscle tissue,[43] ligaments,[44–46] tendons,[24,47] cartilage,[48,49] arteries[50] and membranes.[51] As noted by De Pascalis *et al.*,[21] QLV has been criticised for not always exhibiting "physically reasonable behaviour." In that article, the authors thoroughly reappraised the theory and elucidated that its supposed unphysical behaviour stemmed from different interpretations of Fung's original one-dimensional relationship. The main deficiencies in these anterior studies, as summarised by De Pascalis *et al.*,[52] were using an incorrect QLV relation (especially for incompressible materials) and employing a stress measure other than the second Piola–Kirchhoff stress, which guarantees objectivity. Using the reappraised QLV model (subsequently referred to as modified quasi-linear viscoelasticity or MQLV), De Pascalis *et al.* studied uniaxial tension[21] and simple shear,[52] while Righi and Balbi[53] considered torsion. Balbi *et al.*[54,55] extended the model to transversely isotropic materials. In contrast to Fung's QLV model, the MQLV model has yet to be validated with experimental data. To the authors' knowledge, the only relevant example is the paper by De Pascalis *et al.*,[56] which demonstrated that the MQLV model provided a better fit to the relaxation data from inflation tests on murine bladders compared to Fung's model or linear viscoelasticity. Consequently, MQLV's potential for model fitting and material parameter estimation has yet to be fully exploited.

The development of testing protocols to characterise brain tissue's viscoelastic properties presents numerous challenges.[1,23] For instance, brain tissue's fragile, brittle and tacky nature makes it susceptible to damage during sample preparation and testing.[1] Furthermore, brain tissue is highly compliant and ultra-soft, which can lead to significant deformation under the action of its own weight, making it difficult to control sample geometry during extraction and testing.[1] Additionally, the forces measured during testing often approach the resolution limits of commercially available testing equipment. All these factors and others—for example, age,[57] species,[57] anatomical region,[58] post-mortem storage time[59] and temperature[60,61]—may contribute to the variations in the mechanical properties of brain tissue reported in the literature.

Budday *et al.*[1] and Chatelin *et al.*[23] provide extensive reviews of the viscoelastic properties of brain tissue as measured in various studies, drawing on over 50 years of research in brain mechanics. These studies demonstrate that stress relaxation in brain tissue has been tested under various deformation modes, including uniaxial tension,[5] uniaxial compression,[7] simple shear[6] and torsion.[62] Typically, uniaxial tension and compression tests on brain tissue are performed by glueing the ends of a cylindrical sample to the platens,[5,7] restricting lateral expansion or contraction at the sample's ends. This restriction leads to inhomogeneous deformations,[5,63] which cannot be accurately modelled using the analytical solutions available for such tests;[21] instead, the equations of motion must be solved numerically, complicating model fitting. By contrast, compression tests with lubricated platens can achieve homogeneous deformation conditions but only up to a strain of approximately 10%.[2,5] Another standard testing protocol for brain tissue that can achieve a stretch of more than 60% is simple shear, which is performed by glueing the opposite faces of a cuboidal sample to the platens and recording the shear and normal forces required to move one platen parallel to the other.[3] Additionally, surface tractions must be applied to the slanted faces of the deformed sample to prevent bending.[64] In reality, these tractions are never applied; more practically, the effect of deviation from ideal simple shear conditions on the measured shear and normal forces is minimised by using a thin sample whose width is less than four times its height.[3,6,64,65] Furthermore, accurately quantifying the normal force is currently neither feasible nor practical, as it requires recently developed, custom-designed testing equipment.[64,66] Thus, in practice, simple shear generates a single dataset for the shear force, similar to uniaxial tension or compression tests that produce a single dataset for the tensile or compressive force. Alternatively, torsion is a more robust and reliable testing protocol that can be readily implemented for brain tissue using commercial devices known as rheometers. These devices measure the torque and normal force required to twist a cylindrical sample, generating two independent datasets (the appearance of a normal force as a result of twisting is an example of the so-called Poynting effect[67,68]). The first study to apply this protocol to brain tissue was carried out by Balbi *et al.*,[2] who showed that the instantaneous elastic response of brain tissue in torsion is well-captured by a hyperelastic Mooney–Rivlin model and estimated the corresponding elastic material parameters (the instantaneous shear modulus and Mooney–Rivlin parameters). Although stress relaxation in torsion has been investigated in animal (porcine and bovine) and human brain tissues,[1,23] anterior studies have focused on measuring only the torque, neglecting the normal force. In addition, torsion was modelled

 This journal is © The Royal Society of Chemistry 2025

Open Access Article. Published on 23 May 2025. Downloaded on 6/19/2025 2:26:22 PM. This article is licensed under a Creative Commons Attribution 3.0 Unported Licence.

as simple shear but only locally is the torsion deformation that of simple shear.[2] Consequently, the potential of torsion as a robust and reliable testing protocol for determining the viscoelastic properties of brain tissue has yet to be fully realised. We note that Narayan *et al.*[69] devised a similar protocol for asphalt binders in torsion, measuring both torque and normal force during relaxation. However, to the best of the authors' knowledge, an analogous protocol for soft tissues has yet to be developed.

In this work, we exploit the latent potentials of the torsion protocol and the MQLV model to determine the viscoelastic properties of brain tissue. The remainder of this paper is organised as follows. In Section 2, we describe the procedure for preparing the cylindrical brain samples and testing them with the rotational rheometer, with the results of the torsion tests presented in Section 3. In Section 4, we propose a novel fitting procedure for determining brain tissue's viscoelastic material parameters based on the MQLV model. Following this, we present a finite element implementation of the MQLV model in the open-source software FEniCS, which we use to validate our estimates of the viscoelastic material parameters through numerical simulations of the experiments. We discuss the results and summarise the important features of the paper in Section 5.

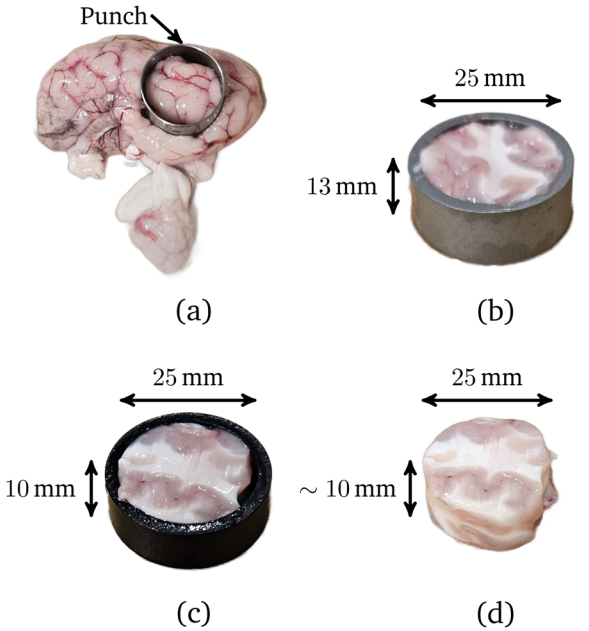

Fig. 1 Procedure for preparing cylindrical brain samples of radius 12.5 mm and height 10 mm for testing: (a) long cylindrical sample excised from the cerebral hemisphere using a steel punch; (b) top face cut flat using a cutting guide of height 13 mm; (c) opposite face cut flat using a cutting guide of height 10 mm and (d) flat cylindrical sample ready for testing.

2 Materials and methods

In this section, we briefly describe the procedure for preparing the cylindrical brain samples and testing them with the rotational rheometer.

2.1 Tissue preparation

All experiments were performed using brains from 6 to 9-month-old, mixed-sex sheep obtained from a local European Union-approved slaughterhouse (Athenry Quality Meats Ltd, Galway, Ireland, Approval Number EC2875). As the animals were not sacrificed specifically for this study, ethical approval was not required from the University of Galway's Research Ethics Committee.

The brains, which were received as separated cerebral hemispheres, were placed in a phosphate buffered saline (PBS) solution within 1 hour post-mortem to avoid tissue dehydration and maintained at 11–15 °C during transportation. All samples were prepared and tested at room temperature (19–23 °C). As shown in Fig. 1(a), mixed grey and white matter cylindrical samples were excised from the sagittal plane using a sharp 25 mm diameter stainless steel punch, with at most two samples extracted from each cerebral hemisphere: one from the frontal portion and the other from the parietal portion. To prepare flat cylindrical samples of radius R_0 = 12.5 mm and height H_0 = 10 mm for testing, each long sample was first inserted into a cutting guide of height 13 mm. The excess brain matter was then removed from the top of the sample using an 8 inch MacroKnife (CellPath, Wales, United Kingdom), as shown in Fig. 1(b). Finally, the opposite end of the sample was cut flat with the aid of a cutting guide of height 10 mm, as shown in Fig. 1(c); the exact heights of the samples were measured before testing. After this, the prepared sample and cerebral hemisphere were placed in a PBS solution. Instead of preparing all the samples at once, each sample was tested immediately after preparation, and then, if possible, another was extracted from the cerebral hemisphere.[6] All samples were tested within 8 hours post-mortem.

2.2 Mechanical testing

An Anton Paar MCR 302e rotational rheometer with parallel plate geometry (Anton Paar, Graz, Austria) was used for the mechanical testing (see Fig. 2). During the tests, the bottom Peltier plate remained fixed, while the motion of the upper plate (which contains the motors and sensors that measure the torque and normal force) was controlled through the software RheoCompass (Version 1.31). A 25 mm diameter upper plate was used, matching the dimension of the samples tested. Masking tape of negligible thickness compared to the sample height was applied to both plates to prevent damage to the rheometer and enable easy removal of the tested samples.[2,5,6] The sample was secured to the tape using a thin layer of cyanoacrylate (RS Radionics, Dublin, Ireland).[5–7] A small pre-compression of approximately 0.03 N was applied by manually lowering the upper plate to ensure proper sample adhesion to the upper and lower plates. Ninety seconds was sufficient time for the glue to set, after which the position of the upper plate was slowly adjusted until the normal force read 0 N.

Our torsion testing protocol is summarised in Table 1 and illustrated in Fig. 3. We performed three sets of ramp-and-hold relaxation tests in torsion on the cylindrical samples at varying twist rates of $\dot{\phi}_0 \in \{40, 240, 400\}$ rad m^{-1} s^{-1} (angular velocity of the upper plate per unit deformed height), while keeping the twist fixed at ϕ_0 = 88 rad m^{-1} (angle of rotation per unit

Open Access Article. Published on 23 May 2025. Downloaded on 6/19/2025 2:26:22 PM.
This article is licensed under a Creative Commons Attribution 3.0 Unported Licence.

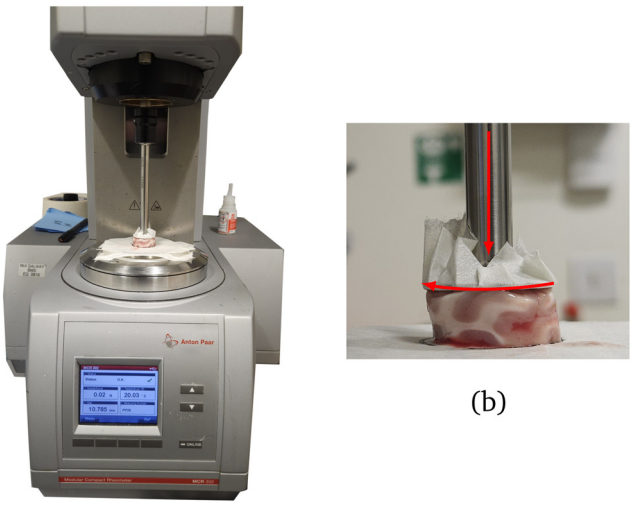

Fig. 2 (a) Anton Paar MCR 302e rotational rheometer with parallel plate geometry used to perform the torsion tests and (b) side view of a twisted sample during testing.

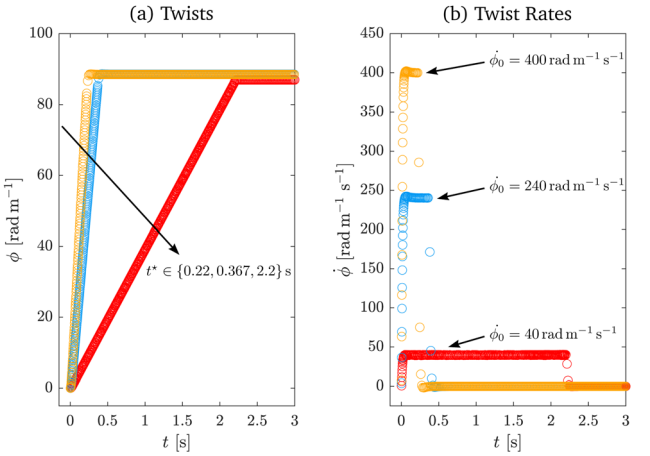

Fig. 3 (a) Twist and (b) twist rate profiles for our proposed torsion testing protocol. The twist for the three sets of tests was increased linearly to a final value of ϕ_0 = 88 rad m^{-1} over durations of $t^\star \in \{2.2, 0.367, 0.22\}$ s, corresponding to twist rates of $\dot{\phi}_0 \in \{40, 240, 400\}$ rad m^{-1} s^{-1} respectively. After reaching the final twist value, the twist was held constant for 200 s.

deformed height). Each torsion test consisted of two phases: a ramp phase, in which the twist was increased linearly to ϕ_0 = 88 rad m^{-1} over a time $t^\star \in \{2.2, 0.367, 0.22\}$ s, followed by a hold phase lasting 200 s, during which the final value of the twist reached at the end of the ramp phase was maintained. Both the torque τ and normal force N_z required to twist the sample during the ramp phase and maintain the sample in its deformed state during the hold phase were recorded *versus* time t. No preconditioning was performed on the samples, and each was tested only once before being discarded. A total of 30 samples were tested over several campaigns: 10 at 40 rad m^{-1} s^{-1} (samples S_1 to S_{10}); 10 at 240 rad m^{-1} s^{-1} (samples S_{11} to S_{20}) and 10 at 400 rad m^{-1} s^{-1} (samples S_{21} to S_{30}).

3 Experimental results

In this section, we present representative torque and normal force data from the rheometer for each of the twist rates $\dot{\phi}_0 \in \{40, 240, 400\}$ rad m^{-1} s^{-1} and describe the filtering procedure applied to the data to prepare it for model fitting and material parameter estimation.

As an example, the output data for sample S_{16}, recorded during a torsion test performed at a twist rate of $\dot{\phi}_0$ = 240 rad m^{-1} s^{-1}, are presented in Fig. 4. Fig. 4(a) and (b) show the twist ϕ and twist rate $\dot{\phi}$ profiles for the test, while Fig. 4(c) and (d) display the measured torque τ and Fig. 4(e) and (f) the measured normal force N_z. Since the rheometer outputs the normal force exerted by the sample on the upper plate, we changed the sign of the data so that it represents the normal force that must be applied to the sample to maintain the deformation, consistent with the modelling conventions adopted in Section 4 and anterior studies.[2,53]

From the data presented in Fig. 4(a) and (b), we can identify four regions: (i) a region (black data) at the start of the ramp phase, where the upper plate accelerates from rest to the target twist rate of $\dot{\phi}_0$ = 240 rad m^{-1} s^{-1}; (ii) a region (purple data), where this twist rate is maintained until the twist reaches ϕ_0 = 85 rad m^{-1} at the end of the ramp phase at time $t^\star = 0.367$ s (indicated by a dashed line); (iii) a region (red data) at the start of the hold phase, where the upper plate decelerates to rest and (iv) the remainder (orange data) of the hold phase, where the final value of the twist reached at the end of the ramp phase is maintained. We also note experimental artefacts in the raw torque data in Fig. 4(c) in regions where there is a rapid change in the twist rate—notably at the start of the ramp phase when the upper plate is accelerating (black data) and the start of the hold phase when it is decelerating (red data)—confirmed by conducting control tests without any samples between the plates (see the ESI†). Accordingly, these artefacts—potentially due to the inertia of the motors in the upper plate[69]—were excluded from the torque data in Fig. 4(d). Following the protocol of Balbi *et al.*,[2] we also excluded the raw normal force data at the start of the ramp phase from the normal force data in Fig. 4(f). However, unlike the torque, the raw normal force data generated at the start of the hold phase does not appear to be adversely affected by the rapid change in twist rate and was therefore included in the normal force data.

During the gamut of tests, the achieved twist rates $\dot{\phi}_0$ were measured as 40.26 ± 0.42, 239.95 ± 0.25 and

Table 1 Torsion testing protocol

- Ramp phase: twist increased linearly to ϕ_0 = 88 rad m^{-1} over durations of $t^\star \in \{2.2, 0.367, 0.22\}$ s at twist rates of $\dot{\phi}_0 \in \{40, 240, 400\}$ rad m^{-1} s^{-1}
- Hold phase: twist maintained at ϕ_0 = 88 rad m^{-1} for 200 s

This journal is © The Royal Society of Chemistry 2025

Open Access Article. Published on 23 May 2025. Downloaded on 6/19/2025 2:26:22 PM.
This article is licensed under a Creative Commons Attribution 3.0 Unported Licence.

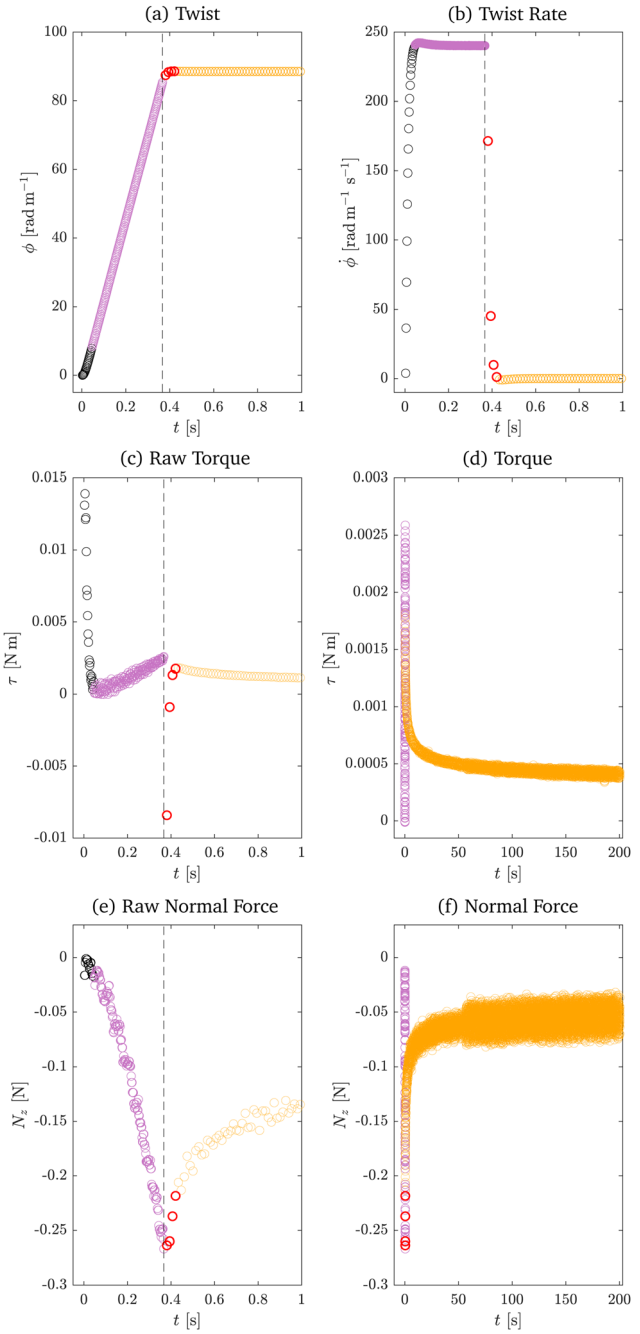

Fig. 4 Output data for sample S_{16} from a torsion test performed at a twist rate of 240 rad m^{-1} s^{-1}: (a) and (b) twist and twist rate profiles; (c) and (e) measured torque and normal force for the first second of the test (including experimental artefacts) and (d) and (f) measured torque and normal force for the entire duration of the test (excluding experimental artefacts). Both the raw torque data generated when the upper plate was accelerating (black) and decelerating (red) were excluded from the torque data in (c), whereas only the raw normal force data generated when the upper plate was accelerating were excluded from the normal force data in (f). A dashed line indicates the end of the ramp phase.

400.06 ± 0.27 rad m^{-1} s^{-1} (mean ± SD). The corresponding ramp times t^* were set to 2.2, 0.367 and 0.22 s to achieve the target twist of ϕ_0 = 88 rad m^{-1} at the end of the ramp phase. However, in practice, the actual twist values reached were slightly lower and decreased with increasing twist rate: 87.48 ± 0.51, 85.25 ± 0.1 and 83.23 ± 0.1 rad m^{-1}. This discrepancy was due to the inertia of the upper plate, which caused the twist to continue increasing slightly at the start of the hold phase while the upper plate decelerated to rest (see Fig. 4(a)). As a result, the target twist was reached during the hold phase rather than at the end of the ramp phase. This deviation between the target and actual twist values at the end of the ramp phase is a practical limitation of our protocol.

Following the protocol of Narayan *et al.*,[69] we estimated the rheometer's torque and normal force resolutions to be approximately 0.15 mN m and 0.03 N by performing torsion tests at each of the twist rates {40, 240, 400} rad m^{-1} s^{-1} without any samples between the plates. Another source of noise in the experiments was the attached compressor, which was required for the proper operation of the rheometer. During each test, the compressor would activate to supply fresh compressed air to the air bearings of the rheometer's motors, generating vibrations that increased the noise in the torque and normal force measurements (see Fig. 4(d) and (f) at $t \approx 50$ s). In preparation for model fitting, we smoothed the data by applying a Savitzky–Golay filter using the MATLAB (Version 23.2.0.2485118 (R2023b)) function sgolayfilt.[70] For the 40 rad m^{-1} s^{-1} data, we used a polynomial order of 5 and a window length of 61, whereas for the 240 and 400 rad m^{-1} s^{-1} data, we used a polynomial order of 5 and a window length of 31 (see the ESI†). Fig. 5 shows representative torque, normal force and filtered data for samples S_2, S_{16} and S_{24} at each twist rate.

4 Modelling

In this section, we use the MQLV theory to derive analytical expressions for the torque and normal force for a ramp-and-hold test. We then propose a fitting procedure for determining brain tissue's viscoelastic material parameters and apply it to the experimental data. Finally, to validate our fitting results, we perform numerical simulations of the experiments in FEniCS.

4.1 Theory

Here, we calculate the torque and normal force required to maintain an isotropic, incompressible, viscoelastic cylinder in a state of torsion, according to the MQLV theory. Although brain tissue is neither strictly isotropic nor incompressible, experiments indicate these are reasonable assumptions.[1]

We consider a cylinder of radius R_0 and height H_0 subjected to a torsional deformation that takes the point with cylindrical polar coordinates (R,Θ,Z) in the undeformed configuration (at time $t = 0$) to the point with cylindrical polar coordinates (r,θ,z) in the deformed configuration (at time $t > 0$), both relative to a fixed origin O. Since the rheometer's normal force sensor has a resolution of approximately 0.03 N, the device cannot detect variations of the normal force within this range. We, therefore, expect the samples to undergo a slight axial contraction before being twisted, even though the upper plate is adjusted until the normal force reads 0 N before each

Open Access Article. Published on 23 May 2025. Downloaded on 6/19/2025 2:26:22 PM.
This article is licensed under a Creative Commons Attribution 3.0 Unported Licence.

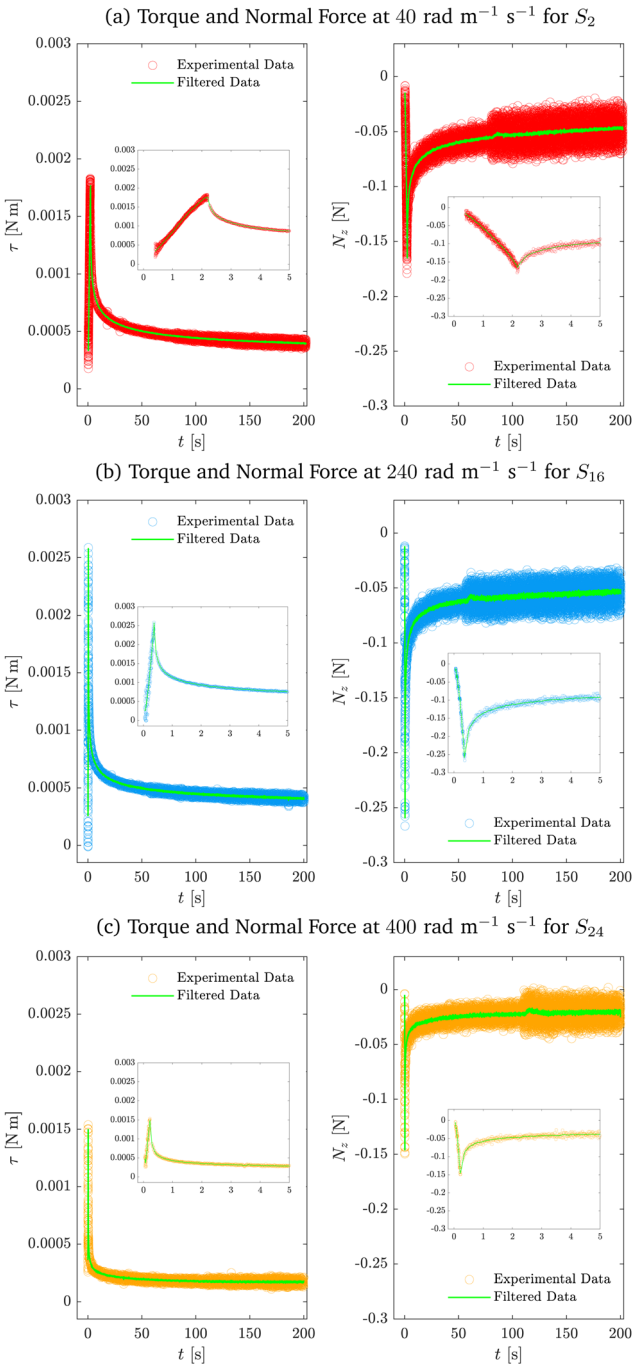

Fig. 5 Representative torque, normal force and filtered data for samples (a) S_2, (b) S_{16} and (c) S_{24} from torsion tests performed at twist rates of {40, 240, 400} rad m^{-1} s^{-1}. The insets show the ramp phase and the initial part of the hold phase in more detail.

test.[2] This combined contraction–torsion can be modelled by the following deformation:[2,71]

$$r(t) = \frac{R}{\sqrt{\lambda}}, \quad \theta(t) = \Theta + \lambda\phi(t)Z, \quad z(t) = \lambda Z, \qquad (1)$$

where $0 < \lambda \leq 1$ is the (axial) pre-stretch and the twist $\phi(t) = \alpha(t)/\lambda H_0$ is the angle of rotation α per unit deformed height (see

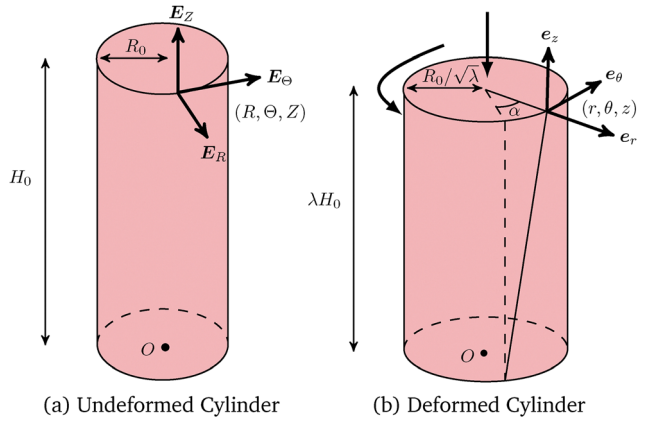

Fig. 6 (a) Undeformed and (b) deformed cylinder. Torque and normal force must be applied at the end of the cylinder to maintain the torsion deformation.

Fig. 6). The pure torsion case ($\lambda = 1$) was considered by Righi and Balbi.[53] By introducing the cylindrical bases $\{\boldsymbol{E}_R, \boldsymbol{E}_\Theta, \boldsymbol{E}_Z\}$ and $\{\boldsymbol{e}_r, \boldsymbol{e}_\theta, \boldsymbol{e}_z\}$ for the undeformed and deformed configurations, we can write the deformation gradient $\boldsymbol{F} = F_{aA}\boldsymbol{e}_a \otimes \boldsymbol{E}_A$ associated with the deformation (1) as follows:

$$\boldsymbol{F}(r,t) = \begin{pmatrix} \frac{1}{\sqrt{\lambda}} & 0 & 0 \\ 0 & \frac{1}{\sqrt{\lambda}} & r\lambda\phi(t) \\ 0 & 0 & \lambda \end{pmatrix}. \qquad (2)$$

Various tensors can be computed from the deformation gradient, such as the left Cauchy–Green deformation tensor $\boldsymbol{B} = \boldsymbol{F}\boldsymbol{F}^{\mathrm{T}}$ and right Cauchy–Green deformation tensor $\boldsymbol{C} = \boldsymbol{F}^{\mathrm{T}}\boldsymbol{F}$.

In their experimental study, Balbi *et al.*[2] showed that the instantaneous elastic response of brain tissue in torsion is well-captured by a Mooney–Rivlin strain energy function:[21,72,73]

$$W^{\mathrm{e}} = \frac{\mu_0}{2}\left(\frac{1}{2} + \gamma\right)(I_1 - 3) + \frac{\mu_0}{2}\left(\frac{1}{2} - \gamma\right)(I_2 - 3), \qquad (3)$$

where μ_0 is the instantaneous shear modulus, γ is a constant, $I_1 = \mathrm{tr}\,\boldsymbol{B}$ and $I_2 = \mathrm{tr}\,\boldsymbol{B}^{-1}$. For this model, the Mooney–Rivlin parameters c_1 and c_2 are connected to μ_0 and γ through $\mu_0 = 2(c_1 + c_2)$ and $\gamma = 1/2 - 2c_2/\mu_0$. The same Mooney–Rivlin behaviour was observed in simple shear[3] and at dynamic strain rates in simple shear,[6] uniaxial tension[5] and uniaxial compression.[7] Under our assumptions, the elastic Cauchy stress corresponding to (3) reads:[74,75]

$$\boldsymbol{T}^{\mathrm{e}} = \frac{\mu_0}{2}(1 + 2\gamma)\boldsymbol{B} - \frac{\mu_0}{2}(1 - 2\gamma)\boldsymbol{B}^{-1} - p^{\mathrm{e}}\boldsymbol{I}, \qquad (4)$$

where p^{e} is the elastic Lagrange multiplier introduced to enforce the incompressibility constraint ($J = \det \boldsymbol{F} = 1$) and $\boldsymbol{I}$ is the second-order identity tensor.

This journal is © The Royal Society of Chemistry 2025

Open Access Article. Published on 23 May 2025. Downloaded on 6/19/2025 2:26:22 PM. This article is licensed under a Creative Commons Attribution 3.0 Unported Licence.

According to the MQLV theory, the viscoelastic Cauchy stress can be expressed as follows:[21,53,56]

$$\boldsymbol{T}(r,t) = \boldsymbol{F}(r,t)\left(\boldsymbol{\Pi}_{\mathrm{D}}^{\mathrm{e}}(r,t) + \frac{1}{\mu_0}\int_0^t \mu'(t-s)\boldsymbol{\Pi}_{\mathrm{D}}^{\mathrm{e}}(r,s)\mathrm{d}s\right)\boldsymbol{F}(r,t)^{\mathrm{T}} - p(r,t)\boldsymbol{I}, \tag{5}$$

where the prime denotes a derivative with respect to the argument of the function and p^{e} has been incorporated into the viscoelastic Lagrange multiplier p, taken to be a function of r and t only without loss of generality.[53] The elastic response in the above is captured by the second Piola–Kirchhoff stress tensor:

$$\begin{aligned}\boldsymbol{\Pi}_{\mathrm{D}}^{\mathrm{e}} &= \boldsymbol{F}^{-1}\boldsymbol{T}_{\mathrm{D}}^{\mathrm{e}}\boldsymbol{F}^{-\mathrm{T}} \\ &= \frac{\mu_0}{3}(1-2\gamma)\boldsymbol{C}^{-1} - \frac{\mu_0}{2}(1-2\gamma)\boldsymbol{C}^{-2} + \frac{\mu_0}{2}(1+2\gamma)\boldsymbol{I},\end{aligned} \tag{6}$$

corresponding to the deviatoric Cauchy stress $\boldsymbol{T}_{\mathrm{D}}^{\mathrm{e}} = \boldsymbol{T}^{\mathrm{e}} - (\mathrm{tr}\,\boldsymbol{T}^{\mathrm{e}}/3)\boldsymbol{I}$, while the time-dependent behaviour is associated with the scalar relaxation function $\mu(t)$, taken to be an n-term Prony series of the form:[6,53,76–78]

$$\mu(t) = \mu_\infty + \sum_{i=1}^{n}\mu_i \mathrm{e}^{-t/\tau_i}, \tag{7}$$

where $\mu(0) = \mu_0$ and μ_∞ are the instantaneous and long-time shear moduli, μ_i are the relaxation coefficients and τ_i are the relaxation times. From (2), (5), (6) and (7), we can determine the components of $\boldsymbol{T}$, shown in the ESI.†

In this work, we assume that the deformation is slow enough that inertial effects can be ignored, although this assumption is not strictly valid during the ramp phase.[55,79] In addition, we neglect external body forces. The motion of the cylinder is therefore governed by the momentum balance equation $\mathrm{div}\,\boldsymbol{T} = \boldsymbol{0}$, where div is the divergence operator in the deformed configuration.[74,75] Upon inspection of the components of the equation of motion, and assuming that the lateral surface of the cylinder is traction-free, we arrive at the following equilibrium problem:[53]

$$\begin{cases}\dfrac{\partial T_{rr}(r,t)}{\partial r} + \dfrac{T_{rr}(r,t) - T_{\theta\theta}(r,t)}{r} = 0, \\ T_{rr}(R_0,t) = 0.\end{cases} \tag{8}$$

By integrating $(8)_1$ subject to $(8)_2$, we can determine the Lagrange multiplier p (see the ESI†).

Given the expressions for the stress components $T_{\theta z}$ and T_{zz} in the ESI,† the torque $\tau(t) = 2\pi\int_0^{R_0/\sqrt{\lambda}} r^2 T_{\theta z}(r,t)\mathrm{d}r$ and normal force $N_z(t) = 2\pi\int_0^{R_0/\sqrt{\lambda}} r T_{zz}(r,t)\mathrm{d}r$ required to maintain the deformation (1) can be determined by direct integration, with explicit expressions shown in the ESI.† Specialising these equations to a ramp-and-hold test, which corresponds to a twist history of the form (see Fig. 3(a)):

$$\phi(t) = \begin{cases}\dfrac{\phi_0 t}{t^\star}, & 0 \le t \le t^\star \\ \phi_0, & t > t^\star,\end{cases} \tag{9}$$

we find that the torque and normal force during the hold phase ($t > t^\star$) read respectively:

$$\begin{aligned}\tau^{\mathrm{hold}}(t) = {}& \frac{\pi\mu_\infty R_0^4}{4}A(\lambda,\gamma)\phi_0 + \frac{\pi R_0^4}{12\lambda^3 t^\star}A(\lambda,\gamma)\sum_{i=1}^{n}\mu_i \mathrm{e}^{-t/\tau_i}\left[2\left(\lambda^3-1\right)t^\star\right. \\ &\left. + \left(\lambda^3+2\right)\tau_i\left(\mathrm{e}^{t^\star/\tau_i}-1\right)\right]\phi_0 + \frac{\pi R_0^6}{18\lambda t^{\star 3}}B(\lambda,\gamma) \\ &\times\sum_{i=1}^{n}\mu_i\tau_i \mathrm{e}^{-t/\tau_i}\left[-2\tau_i(t^\star+3\tau_i) + \mathrm{e}^{t^\star/\tau_i}\left(t^{\star 2} - 4\tau_i t^\star + 6\tau_i^2\right)\right]{\phi_0}^3\end{aligned} \tag{10}$$

and

$$\begin{aligned}N_z^{\mathrm{hold}}(t) = {}& \pi\mu(t)R_0^2\left(\frac{\lambda^3-1}{2\lambda^2}\right)A(\lambda,\gamma) - \frac{\pi\mu_\infty R_0^4}{8}B(\lambda,\gamma){\phi_0}^2 \\ &- \frac{\pi R_0^4}{12\lambda^4 t^{\star 2}}\sum_{i=1}^{n}\mu_i \mathrm{e}^{-t/\tau_i}\left[(1-2\gamma)\left\{\mathrm{e}^{t^\star/\tau_i}\left(3\lambda^3\tau_i t^\star - C(\lambda)\tau_i^2\right)\right.\right. \\ &\left. - D(\lambda)t^{\star 2} + E(\lambda)\tau_i t^\star + C(\lambda)\tau_i^2\right\} \\ &+ 2\lambda\left(\lambda^3+2\right)\tau_i^2\mathrm{e}^{t^\star/\tau_i} + 2\lambda\left(\lambda^3-1\right)t^{\star 2} \\ &\left. - 2\lambda\left(\lambda^3+2\right)\tau_i t^\star - 2\lambda\left(\lambda^3+2\right)\tau_i^2\right]{\phi_0}^2 \\ &- \frac{\pi R_0^6}{18\lambda t^{\star 4}}B(\lambda,\gamma)\sum_{i=1}^{n}\mu_i\tau_i^2\mathrm{e}^{-t/\tau_i}\left[\mathrm{e}^{t^\star/\tau_i}\left(t^{\star 2} - 6\tau_i t^\star + 12\tau_i^2\right)\right. \\ &\left. - t^{\star 2} - 6\tau_i t^\star - 12\tau_i^2\right]{\phi_0}^4,\end{aligned} \tag{11}$$

where the expressions for the functions A, B, C, D and E are given in Appendix A. Analogous expressions for the ramp phase ($0 \le t \le t^\star$) are shown in the ESI.† The results of Righi and Balbi[53] are recovered by setting $\lambda = 1$.

4.2 Material parameter estimation

Righi and Balbi[53] proposed a fitting procedure for estimating brain tissue's viscoelastic properties in torsion based on the MQLV model for the case when there is no pre-stretch ($\lambda = 1$). In their method, the material parameters μ_∞ and c_2 are determined from the long-time (asymptotic) values of the torque and normal force, while μ_i and τ_i are obtained by fitting the measured torque for the hold phase to the MQLV analytical prediction. Since this procedure does not incorporate a pre-stretch, an alternative fitting procedure that accounts for the effect of pre-stretch on the torque and normal force is required to fit the experimental data accurately.

To this end, we estimated the complete set of viscoelastic material parameters by simultaneously fitting the torque and normal force datasets for each of the twist rates $\dot{\phi}_0 \in \{40, 240, 400\}$ rad m^{-1} s^{-1} to the MQLV analytical predictions (10) and (11). This was done using the MATLAB function fmincon,[80] which implements an algorithm based on the interior-point method for solving constrained non-linear optimisation problems. Due to the increased noise during the ramp phase, we confined the fitting to the final ramp phase point and the entire

Open Access Article. Published on 23 May 2025. Downloaded on 6/19/2025 2:26:22 PM.
This article is licensed under a Creative Commons Attribution 3.0 Unported Licence.

hold phase, *i.e.* $t \geq t^*$. For the twists ϕ_0, we used the measured values at the end of the ramp phase rather than the target value. We minimised the following objective function:

$$\chi^2 = \sum_{i=1}^{n_1} \left(\frac{\tau_i^{\mathrm{MQLV}} - \tau_i^{\mathrm{Exp}}}{\tau_i^{\mathrm{Exp}}} \right)^2 + \sum_{i=1}^{n_2} \left(\frac{N_{z,i}^{\mathrm{MQLV}} - N_{z,i}^{\mathrm{Exp}}}{N_{z,i}^{\mathrm{Exp}}} \right)^2, \quad (12)$$

where n_1 and n_2 are the numbers of considered torque and normal force datapoints τ_i^{Exp} and $N_{z,i}^{\mathrm{Exp}}$, while τ_i^{MQLV} and $N_{z,i}^{\mathrm{MQLV}}$ are the corresponding MQLV analytical predictions. This method is similar to that used by Anssari-Benam *et al.*[81] The advantage of this approach, which minimises the relative error, over the more common approach of minimising the absolute error was discussed by Destrade *et al.*[82] We estimated the Prony parameters (μ_∞, μ_i and τ_i) from a 4-term Prony series. The rationale for choosing $n = 4$ was that it was the minimum number of terms needed to accurately replicate the relaxation curves for the torque and normal force across all samples and was therefore the least computationally expensive choice for the present application. This is in line with previous studies, in which 2-, 3- or 4-term Prony series were used to model stress relaxation in brain tissue.[77,78] To ensure that the fitting results were physically plausible, we constrained the Prony and Mooney–Rivlin parameters to be positive and limited the pre-stretch to no more than 1%.

From each fit, we obtain 10 independent parameters: μ_∞, μ_i, τ_i and γ. We then calculate *a posteriori* the instantaneous shear modulus using $\mu_0 = \mu_\infty + \sum_{i=1}^{4} \mu_i$ and the two Mooney–Rivlin parameters using $c_2 = \mu_0(1/2 - \gamma)/2$ and $c_1 = \mu_0/2 - c_2$. The fitting results for each of the twist rates are shown in Tables 2–4, with the *a posteriori* calculated parameters highlighted in bold. For each sample, we found that $c_2 \gg c_1$, implying that $\mu_0 \approx 2c_2$ and consequently $\gamma \approx -0.5$. Therefore, for brevity, the γ values were omitted from the tables. For the parameters μ_0, μ_∞, μ_i and c_2, we report the mean and standard deviation. For the remaining parameters τ_i and c_1, which have a non-symmetric distribution due to potential outliers, we report the median and interquartile range (IQR). The goodness of fit was assessed based on the relative errors (%) in the torque and normal force, defined by $\mathrm{err}_\tau = |(\tau^{\mathrm{MQLV}} - \tau^{\mathrm{Exp}})/\tau^{\mathrm{Exp}}| \times 100$ and $\mathrm{err}_{N_z} = |(N_z^{\mathrm{MQLV}} - N_z^{\mathrm{Exp}})/N_z^{\mathrm{Exp}}| \times 100$. The MQLV model provides good fits to both the torque and normal force datasets simultaneously, exhibiting small to moderate maximal relative errors over the fitting range for all samples, with the exception of S_{24} (see Tables 2–4). We note that the relative errors observed here for the MQLV model are similar to those reported by Anssari-Benam *et al.*,[81] who simultaneously fit uniaxial tension/compression and simple shear datasets for brain tissue to different hyperelastic models.

As an example, Fig. 7 shows the MQLV analytical predictions for the torque and normal force for samples S_2, S_{16} and S_{24}, while Fig. 8 displays the corresponding relative errors. As the insets in Fig. 8 indicate, the relative errors in the torque are initially moderate to large but rapidly decrease towards the end of the ramp phase. By contrast, the relative errors in the force during the ramp phase are small to moderate. Over the fitting range, comprised of the final ramp phase point and the entire

Table 2 Heights, estimated MQLV parameters and maximal relative errors in the torque and normal force over the fitting range for samples tested at 40 rad m^{-1} s^{-1}

Sample	H_0 [mm]	λ	μ_0 [Pa]	μ_∞ [Pa]	μ_1 [Pa]	μ_2 [Pa]	μ_3 [Pa]	μ_4 [Pa]	τ_1 [s]	τ_2 [s]	τ_3 [s]	τ_4 [s]	c_1 [μPa]	c_2 [Pa]	max err_τ $_{t\geq t^*}$ [%]	max err_{N_z} $_{t\geq t^*}$ [%]
S_1	9.4065	0.99	**651.16**	105.67	213.34	192.34	85.831	53.892	0.8397	0.244	6.4136	55.312	**0.10225**	**325.58**	11.609	16.054
S_2	8.8319	0.99	**917.69**	125.55	606.76	111.28	73.07	1.0213	0.6811	9.5764	82.406	48.45	**2.0793**	**458.84**	13.725	18.992
S_3	8.7603	0.99	**973.9**	128.37	583.34	95.025	91.207	75.954	0.443	9.4962	2.3379	75.888	**0.4711**	**486.95**	13.415	18.628
S_4	9.2659	0.99	**1048**	142.97	628.57	110.42	91.321	74.705	0.4005	2.398	10.442	72.484	**0.13183**	**523.99**	14.281	19.4
S_5	8.9006	0.99	**1308.8**	161.91	455.32	455.31	137.22	99.052	0.6455	0.1715	5.9739	58.745	**0.021216**	**654.41**	18.485	25.642
S_6	9.3734	0.99	**581.02**	64.313	368.49	66.885	44.183	37.148	0.3159	1.782	8.4904	65.141	**1.5548**	**290.51**	10.915	17.506
S_7	8.3203	0.99	**1195.4**	116.2	816.85	137.58	70.991	53.785	0.3639	2.5286	10.9	63.17	**0.028749**	**597.7**	14.239	19.997
S_8	8.4103	0.99	**739.23**	107.05	258.68	242.45	76.34	54.709	0.194	0.7838	6.3087	43.982	**0.003838**	**369.61**	15.575	28.523
S_9	7.9813	0.99	**1216**	149.53	704.25	187.15	103.02	72.031	0.3057	1.9388	10.93	78.995	**0.0094199**	**607.99**	15.803	21.589
S_{10}	8.3523	0.99	**754.36**	71.934	437.68	151.71	55.116	37.911	0.2027	1.1376	8.1273	58.425	**4.2268**	**377.18**	12.582	21.687
Mean ± SD/ Median (IQR)	—	—	**943** ± **258**	117 ± 32	496 ± 177	188 ± 114	85 ± 26	57 ± 27	0.36(0.25–0.59)	1.52(0.87–2.28)	8.15(6.33–9.95)	58.59(55.42–70.65)	**0.3(0.041–1.36)**	**471** ± **129**	14.06 ± 2.2	20.8 ± 3.78

Open Access Article. Published on 23 May 2025. Downloaded on 6/19/2025 2:26:22 PM.
This article is licensed under a Creative Commons Attribution 3.0 Unported Licence.

hold phase, the relative errors in both the torque and normal force are similarly small to moderate. The exception is sample S_{24}, where the relative error in the torque at the start of the hold phase increases sharply before decreasing at a similar rate. This is likely due to the high twist rate of 400 rad m^{-1} s^{-1} and deviations from the ideal cylindrical geometry assumed by the rheometer and MQLV model. Nevertheless, the relative errors for the remainder of the hold phase are in line with those of samples S_2 and S_{16}.

4.3 Computational validation

To validate the fitting results from Section 4.2, we conducted brain torsion simulations using the open-source software FEniCS.[83,84] FEniCS provides a high-level Python and C++ interface for solving partial differential equations *via* the finite element method. For the numerical implementation of the problem, the governing equations for the torsion of a solid cylinder were expressed in Cartesian coordinates and formulated using a Lagrangian description of motion, where all quantities of interest are represented in material coordinates.

In this framework, the governing equations are written as $\mathrm{Div}\,\boldsymbol{P} = \mathbf{0}$ on the undeformed cylinder, where Div represents the divergence operator with respect to the undeformed configuration and $\boldsymbol{P} = J\boldsymbol{T}\boldsymbol{F}^{-\mathrm{T}}$ denotes the first Piola–Kirchhoff stress tensor.[74,75] To enforce incompressibility, we included the constraint $J = 1$ in the model. Before applying torsion, an initial step was introduced to simulate pre-compression, involving an axial pre-stretch of $\lambda = 0.99$. For the torsion simulation, a reference point at the centre of the cylinder's top surface was defined and coupled to all other points on the top surface to ensure uniform rotational displacement about the longitudinal axis. Appropriate boundary conditions were applied as follows: the bottom surface of the cylinder was fixed to prevent displacement, while the lateral surface remained traction-free throughout the simulation.

Numerical simulations were performed for samples S_2, S_{16} and S_{24} at twist rates of {40, 240, 400} rad m^{-1} s^{-1}. The twist was ramped linearly to match experimental values at the end of the ramp phase over time periods of {2.2, 0.367, 0.22} s, after which it was held constant (see Fig. 3). The initial cylindrical geometry for each sample was defined with a radius of R_0 = 12.5 mm, while the heights H_0 were specified in Tables 2–4. Computational meshes were generated in FEniCS, consisting of 16 809, 17 391 and 12 547 tetrahedral elements for the respective samples. Although the same mesh density was prescribed for the first two models, the total number of elements differed due to variations in sample height. For the third sample, the mesh density was slightly reduced to manage the increased computational cost caused by a higher twist rate. To enable a solution *via* the finite element method, the weak formulation of the Lagrangian model was derived and a spatial discretisation of the continuous variational problem was introduced. Specifically, quadratic tetrahedral elements $\mathbb{P}_2$ were employed for the displacement field, while linear tetrahedral elements $\mathbb{P}_1$ were used for the pressure field. This combination is commonly referred to as Taylor–Hood elements, selected to prevent the

Table 3 Heights, estimated MQLV parameters and maximal relative errors in the torque and normal force over the fitting range for samples tested at 240 rad m^{-1} s^{-1}

Sample	H_0 [mm]	λ	$\boldsymbol{\mu_0}$ [Pa]	μ_∞ [Pa]	μ_1 [Pa]	μ_2 [Pa]	μ_3 [Pa]	μ_4 [Pa]	τ_1 [s]	τ_2 [s]	τ_3 [s]	τ_4 [s]	$\boldsymbol{c_1}$ [μPa]	$\boldsymbol{c_2}$ [Pa]	$\max_{\geq r^*} \mathrm{err}_\tau$ [%]	$\max_{\geq r^*} \mathrm{err}_{N_z}$ [%]
S_{11}	8.1853	0.99	**1020**	88.511	359.74	359.41	132.2	80.179	0.1117	0.0941	1.2096	20.497	**91.948**	**510.02**	19.497	18.886
S_{12}	8.7724	0.99	**861.35**	105.47	334.31	315.94	61.799	43.828	0.12	0.5626	17.937	19.834	**1.39**	**430.68**	30.806	31.609
S_{13}	8.8588	0.99	**1253.8**	177.06	740.79	194.66	141.29	3.9931 $\times 10^{-4}$	0.209	2.9542	38.93	18.451	**10.197**	**626.9**	18.992	22.226
S_{14}	9.9285	0.99	**714.17**	107.18	181.16	154.9	153.56	117.37	0.4112	0.4929	0.259	15.306	**28.933**	**357.08**	35.938	31.804
S_{15}	9.7461	0.99	**809.24**	110.98	267.8	240.32	108.64	81.494	0.2705	0.1037	2.187	28.974	**6.2476**	**335.51**	23.35	30.089
S_{16}	9.4673	0.99	**1264.4**	148.86	431.27	399.57	170.89	113.81	0.1179	0.2148	1.7763	25.905	**11.289**	**632.2**	22.962	26.81
S_{17}	9.4488	0.99	**941.46**	142.06	605.37	130.48	63.541	0.0062	0.2915	7.3912	89.376	105.57	**1.3055**	**470.73**	28.384	34.375
S_{18}	11.341	0.99	**1159.5**	134.3	384.24	381.77	161.17	197.97	0.1539	0.1917	2.0081	33.052	**8.7216**	**579.73**	25.468	31.333
S_{19}	8.1197	0.99	**1216**	149.53	704.25	187.15	103.02	72.031	0.3057	1.9388	10.93	78.995	**0.0094199**	**607.99**	22.622	26.891
S_{20}	9.0278	0.99	**1238.3**	168.98	389.22	377.06	171.6	131.48	0.3024	0.1172	2.806	36.611	**2.1066**	**619.17**	21.601	25.781
Mean ± SD/ Median (IQR)	—	—	**1041** ± **201**	130 ± 29	447 ± 198	270 ± 108	126 ± 41	77 ± 66	0.19(0.13–0.27)	0.35(0.14–1.9)	2.5(1.83–29.9)	25.98(20–32.03)	**9.45(3.14–11.02)**	**513** ± **111**	24.96 ± 5.33	27.98 ± 4.8

Open Access Article. Published on 23 May 2025. Downloaded on 6/19/2025 2:26:22 PM.
This article is licensed under a Creative Commons Attribution 3.0 Unported Licence.

Table 4 Heights, estimated MQLV parameters and maximal relative errors in the torque and normal force over the fitting range for samples tested at 400 rad m^{-1} s^{-1}

Sample	H_0 [mm]	λ	μ_0 [Pa]	μ_∞ [Pa]	μ_1 [Pa]	μ_2 [Pa]	μ_3 [Pa]	μ_4 [Pa]	τ_1 [s]	τ_2 [s]	τ_3 [s]	τ_4 [s]	c_1 [μPa]	c_2 [Pa]	max err_{τ} $_{i\geq i^*}$ [%]	max err_{N_z} $_{i\geq i^*}$ [%]
S_{21}	11.402	0.99	**989.56**	116.08	359.18	344.12	170.18	2.3359×10^{-4}	0.114	0.2938	13.187	12.323	**10.829**	**494.78**	29.252	29.349
S_{22}	11.931	0.99	**774.72**	89.185	497.42	113.66	74.464	2.1×10^{-4}	0.185	2.7482	33.279	8.6742	**0.92322**	**387.36**	31.812	40.139
S_{23}	8.5067	0.99	**388.24**	58.62	133.86	123.86	71.964	4.4007×10^{-5}	0.6331	6.4661	40.349	60.757	**0.0059017**	**223.98**	27.018	34.238
S_{24}	10.213	0.99	**920.46**	62.668	535.86	244.75	77.299	0.0013	0.2815	0.0011	12.829	0.9428	**42.44**	**460.23**	69.909	32.426
S_{25}	10.58	0.99	**1379.5**	127.36	370.45	352.02	351.55	178.14	0.0674	0.3406	0.0671	12.155	**0.10553**	**689.77**	30.786	36.412
S_{26}	11.244	0.99	**497.15**	65.435	114.21	114.15	112.31	91.044	0.1048	0.4212	0.397	11.621	**4.0076**	**248.57**	34.013	37.783
S_{27}	8.1004	0.99	**1005.8**	83.491	264.95	260.9	256.02	140.45	0.1004	0.0621	0.317	11.814	**6.3762**	**502.91**	35.692	44.153
S_{28}	8.6911	0.99	**1178.7**	157.1	304.35	274.33	267.27	175.67	0.4461	0.0826	0.0828	14.472	**9.6969**	**589.36**	28.884	30.932
S_{29}	8.8104	0.99	**1495.9**	137.88	512.7	507.84	216.32	121.2	0.0826	0.1105	1.2196	24.011	**3.8003**	**747.97**	19.828	19.538
S_{30}	8.8442	0.99	**1161.9**	125	375.42	374.91	170.68	115.85	0.114	0.1037	0.9253	19.031	**7.6129**	**580.93**	30.257	37.282
Mean	—	—	**979**	102	347	271	177	82	0.11(0.1–0.26)	0.2(0.088–0.4)	1.07(0.34–13.1)	12.24(11.67–17.89)	**5.19(1.64–9.18)**	**493**	33.75	34.23
± SD/ Median (IQR)			**± 354**	± 35	± 147	± 129	± 96	± 75						**± 172**	± 13.41	± 6.78

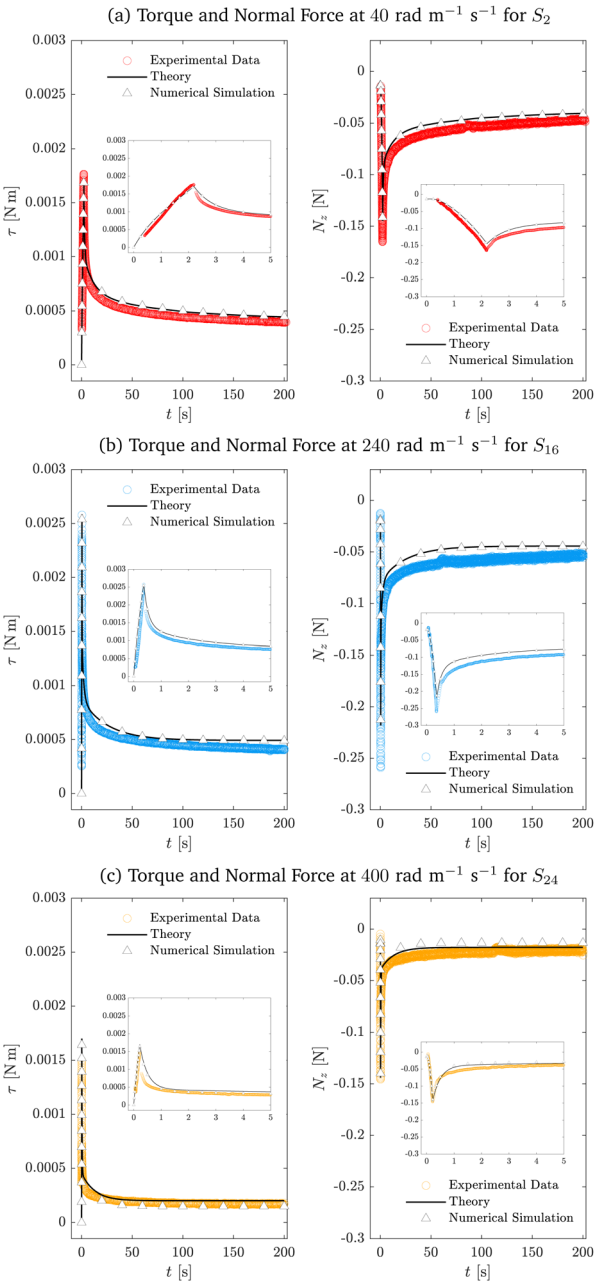

Fig. 7 Comparison of the resultant torque τ and normal force N_z for samples (a) S_2, (b) S_{16} and (c) S_{24} at twist rates of {40, 240, 400} rad m^{-1} s^{-1}. Experimental data are denoted by circles, analytical predictions using the MQLV model by solid black lines and the results of the numerical simulations in FEniCS by triangles. The insets show the ramp phase and the initial part of the hold phase in more detail.

locking phenomenon and ensure stability in simulations involving incompressible materials. This strategy was adopted to avoid the use of hexahedral elements, which, although recognised as an effective method for mitigating volumetric locking, require significantly more complex generation procedures, typically involving external meshing tools and manual intervention, and could not be directly implemented within FEniCS. The time step was initially set to a small value ($\Delta t \in (0.001, 0.01)$ s) during the early simulation phases to accurately capture

This journal is © The Royal Society of Chemistry 2025

Open Access Article. Published on 23 May 2025. Downloaded on 6/19/2025 2:26:22 PM.
This article is licensed under a Creative Commons Attribution 3.0 Unported Licence.

large deformations. As deformation rates decreased, the time step was progressively increased to enhance computational efficiency. The estimated material parameters, determined *via* the MQLV theory, were assigned as specified in Tables 2–4. The torque and normal force were then computed with ParaView,[85] an open-source application for interactive scientific visualisation.

As illustrated in Fig. 7, the torque and normal force computed from the numerical solutions closely align with both the MQLV analytical predictions and the experimental data. However, a slight discrepancy is observed between the analytical predictions and the simulations for sample S_{24}, likely due to the high twist rate of 400 rad m^{-1} s^{-1}. In particular, achieving convergence at high twist rates requires a very small time step, which substantially increases the complexity of the simulations and poses challenges in obtaining accurate results. Finally, in Fig. 9, we present an example of the full 3D simulations, showing the magnitude of the displacement field and the components of the Cauchy stress tensor T_{zz} and $T_{\theta z}$ for sample S_{24} at t = 5 s.

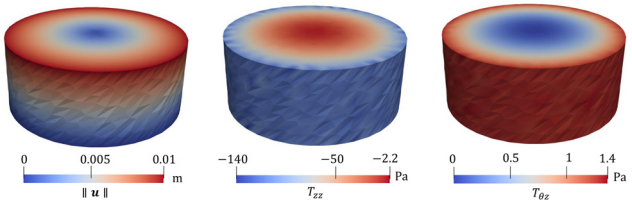

Fig. 9 Comparison of the displacement field magnitude $\|\boldsymbol{u}\|$ and the components of the Cauchy stress tensor T_{zz} and $T_{\theta z}$ for sample S_{24} at t = 5 s.

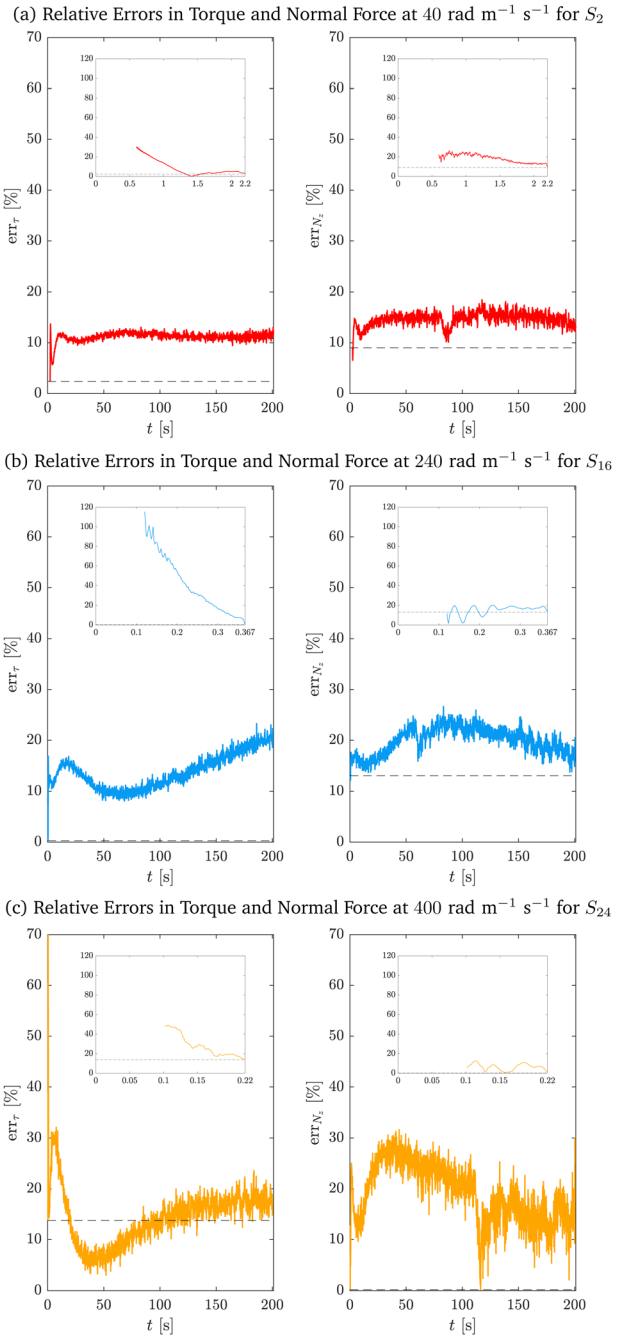

Fig. 8 Relative errors in the torque err_τ and force err_{N_z} for samples (a) S_2, (b) S_{16} and (c) S_{24} at twist rates of {40, 240, 400} rad m^{-1} s^{-1}. The insets show the ramp phase in more detail. The dashed lines indicate the relative errors at the end of the ramp phase.

5 Discussion and conclusions

To investigate the differences between the estimated MQLV parameters at the twist rates {40, 240, 400} rad m^{-1} s^{-1}, we performed Tukey multiple comparisons tests using the R (Version 4.4.2) function TukeyHSD.[86] The column plots in Fig. 10 show that there are no statistically significant differences between the shear moduli and second Mooney–Rivlin parameters at the three twist rates, except for the μ_3 values at 40 rad m^{-1} s^{-1} and 400 rad m^{-1} s^{-1}. By contrast, there are statistically significant differences between several of the relaxation times at the three twist rates (see Fig. 11). However, the statistically significant differences for these Prony parameters may be attributed to their high variability—in particular, the large standard deviations observed for the shear moduli and the wide interquartile ranges for the relaxation times. In practice, the representation of relaxation data by a Prony series is non-unique, with the Prony parameters being highly sensitive to small changes in the data.[20] The apparent strain rate-independence of the material parameters is most likely a consequence of the narrow range of twist rates considered in this study, which fall within the quasi-static to moderate regime. Indeed, the values of μ_0 and c_2 obtained here for ovine brain tissue using the MQLV model are in line with those obtained by Balbi *et al.*[2] for porcine brain tissue at 300 rad m^{-1} s^{-1} using a hyperelastic model. While previous studies have reported a significant increase in brain tissue stiffness with increasing strain rate in uniaxial tension,[5] uniaxial compression[7] and simple shear[6] indicative of a strong strain rate-dependency, the strain rates considered in those studies ({30, 60, 90, 120} s^{-1}) were much higher than those examined here ({0.5, 3, 5} s^{-1}). Nevertheless, the values of μ_0 estimated in this study are comparable to those obtained by Rashid *et al.*[6] for porcine brain tissue from simple shear tests conducted at a strain rate of 30 s^{-1}—a rate conducive to conditions associated with traumatic brain injury (TBI), which typically

Open Access Article. Published on 23 May 2025. Downloaded on 6/19/2025 2:26:22 PM.
This article is licensed under a Creative Commons Attribution 3.0 Unported Licence.

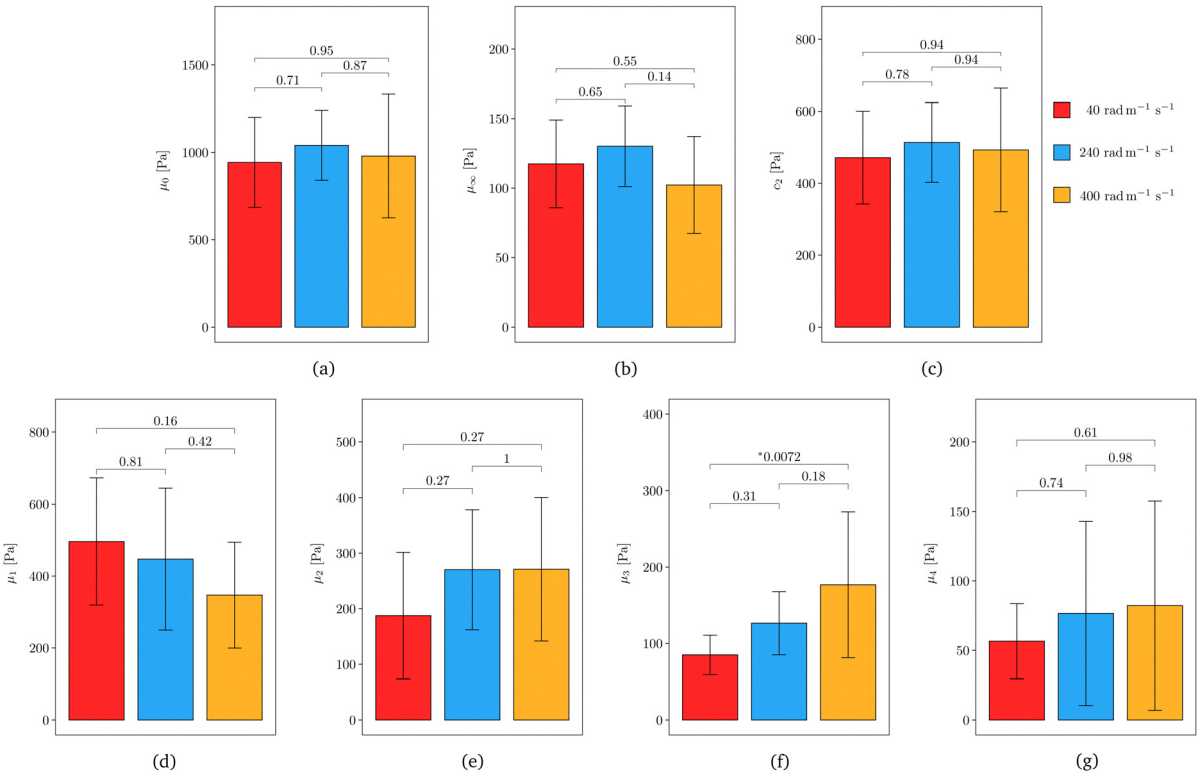

Fig. 10 Column plots (mean ± SD) of the estimated MQLV parameters (a) μ_0, (b) μ_∞, (c) c_2, (d) μ_1, (e) μ_2, (f) μ_3 and (g) μ_4 for samples tested at 40 rad m^{-1} s^{-1} (red), 240 rad m^{-1} s^{-1} (blue) and 400 rad m^{-1} s^{-1} (orange). Also shown are the p-values obtained from Tukey multiple comparisons tests, with asterisks denoting a statistically significant difference ($p < 0.05$).

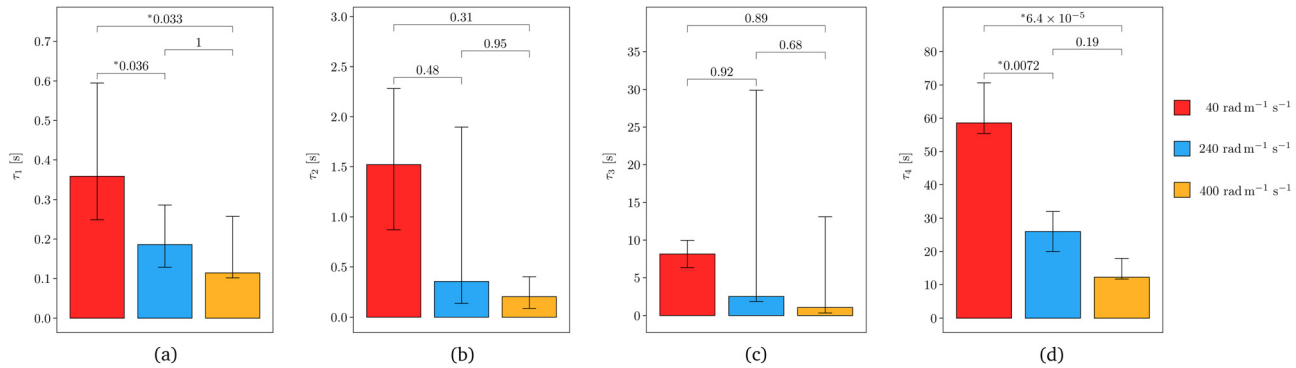

Fig. 11 Column plots (median and IQR) of the estimated MQLV parameters (a) τ_1, (b) τ_2, (c) τ_3 and (d) τ_4 for samples tested at 40 rad m^{-1} s^{-1} (red), 240 rad m^{-1} s^{-1} (blue) and 400 rad m^{-1} s^{-1} (orange). Also shown are the p-values obtained from Tukey multiple comparisons tests, with asterisks denoting a statistically significant difference ($p < 0.05$).

exceed 10 s^{-1}.[6,87,88] Moreover, the strains we considered (~105–110%) are substantially higher than the estimated axonal strain threshold for diffuse axonal injury (~15% for a 50% risk), which is the most prevalent neurological insult associated with TBI.[89] In future work, we will apply our protocol to estimate the material parameters of brain tissue in torsion under conditions more representative of TBI—namely, a minimum strain of 20% applied at a strain rate exceeding 10 s^{-1}.[87,88]

We note in passing that alternative fitting procedures to the one outlined in this study have been proposed in the literature. One common approach that allows for reduced inter-sample variability in the relaxation times involves fixing them *a priori* at logarithmically spaced intervals over the experimental time range, and then employing an optimisation algorithm to determine the remaining parameters.[90,91] See also ref. 92 for a related but more refined procedure.

Our proposed testing protocol presents some challenges and limitations. Due to natural variations in brain size between sheep and brain tissue's highly compliant and ultra-soft nature, it was difficult to consistently and reliably prepare cylindrical

 This journal is © The Royal Society of Chemistry 2025

Open Access Article. Published on 23 May 2025. Downloaded on 6/19/2025 2:26:22 PM. This article is licensed under a Creative Commons Attribution 3.0 Unported Licence.

samples of similar dimensions, as in Fig. 1. As a result, difficult-to-obtain and otherwise useful brain samples were wasted, leading to a smaller sample size. Furthermore, if the samples are not satisfactorily cylindrical (as the rotational rheometer requires), artefacts could potentially be introduced into the measured torque and normal force.

Currently, there is no consensus on the effects of temperature and post-mortem storage time on the mechanical properties of brain tissue.[1] Therefore, it is important to note that the brains in this study were prepared and tested at room temperature (19–23 °C) within 8 hours post-mortem.

Given the limited availability and ethical challenges associated with obtaining fresh human brains in Ireland, ovine brains were used in this work. Despite the widespread use of porcine[2,5,30,62] and bovine[78,93,94] brain tissues as surrogates for characterising the mechanical properties of human brain tissue, there are relatively few studies that focus on ovine brain tissue.[95,96] By contrast, due to the neuroanatomical similarities between the sheep and human brains,[97] there is a growing body of literature that utilises the ovine model to investigate brain injuries, including strokes and epilepsy, among others.[98] Nevertheless, further comparative research is required to determine whether ovine brain tissue—like porcine and bovine brain tissues—is a suitable mechanical surrogate for characterising human brain tissue.

Additionally, in this study, we treated brain tissue as a single homogeneous material. However, brain tissue is known to be highly heterogeneous, with grey and white matter exhibiting markedly different mechanical behaviour.[1,8,9,78] More precise material characterisation could be achieved by applying our testing protocol to grey and white matter samples separately.

Despite the outlined limitations, in this paper, we devised the first experimental protocol to determine the non-linear viscoelastic properties of brain tissue in torsion. This protocol allows us to obtain two independent datasets (torque and normal force) with a single test, providing us with a much more efficient protocol compared to protocols involving multiple loading modes. The latter require a sample to be sequentially tested under different deformation modes to obtain independent datasets. Moreover, they often rely on expensive, custom-made experimental rings or multiple testing devices. Our novel protocol can be easily implemented in any commercially available rheometer and has huge potential to accurately model the non-linear viscoelastic properties of brain tissue.

Here, we applied the protocol to study the non-linear viscoelastic behaviour of the brain in torsion at varying twist rates. This protocol has huge potential not only to study the strain-dependent relaxation of the brain but also its non-linear creep behaviour. From the theoretical viewpoint, we showed that the MQLV model provides a good fit to the experimental data and allows us to estimate the time-dependent shear modulus of an incompressible, viscoelastic, soft material such as the brain. The fitting procedure that we proposed can also be applied to compressible, viscoelastic, soft materials, whose mechanical behaviour is determined by at least two material functions.

In view of the quasi-static to moderate twist rates considered in this study, the estimated viscoelastic material parameters could enhance our understanding of slow-progressing pathologies such as tumour growth or neurodegeneration and inform the development of improved *in silico* models for brain surgery planning and training. More broadly, our novel testing protocol provides a new experimental method that can be applied to measure the viscoelastic properties of soft tissues other than the brain.

As previously discussed, another major direction in future work will be applying our protocol to investigate the mechanical behaviour of brain tissue at conditions conducive to TBI. When coupled with bespoke finite element models such as the University College Dublin Brain Trauma Model,[99] the corresponding viscoelastic material parameters could yield valuable insights into the forces and deformations involved in traumatic brain injury and contribute to the design of improved headgear for sports such as boxing and motorsports.

Author contributions

Griffen Small: investigation, formal analysis, visualization, writing – original draft, writing – reviewing and editing. Francesca Ballatore: investigation, software, visualization, writing – original draft, writing – reviewing and editing. Chiara Giverso: software, visualization, writing – original draft, writing – reviewing and editing. Valentina Balbi: conceptualization, methodology, writing – reviewing and editing.

Data availability

The brain torsion data used in this article has been deposited on Mendeley Data at **https://doi.org/10.17632/m2jwdfgczs.1**. The FEniCS code for the finite element simulations is available on Github at **https://github.com/francescaballatore/Brain_QLV_Torsion**.

Conflicts of interest

There are no conflicts to declare.

Appendices

Appendix A

The functions A, B, C, D and E appearing in the torque (10) and normal force (11) are given by

$$A(\lambda,\gamma)=\frac{1}{\lambda}[\lambda+1+2\gamma(\lambda-1)], \tag{13}$$

$$B(\lambda,\gamma)=\frac{1}{\lambda}[\lambda+2+2\gamma(\lambda-2)], \tag{14}$$

$$C(\lambda)=\lambda^4+2\lambda^3+2\lambda-2, \tag{15}$$

$$D(\lambda)=\lambda^4-\lambda^3-\lambda+1, \tag{16}$$

$$E(\lambda)=\lambda^4-\lambda^3+2\lambda-2. \tag{17}$$

Open Access Article. Published on 23 May 2025. Downloaded on 6/19/2025 2:26:22 PM. This article is licensed under a Creative Commons Attribution 3.0 Unported Licence.

Acknowledgements

This publication has emanated from research jointly funded by Taighde Éireann – Research Ireland under grant number GOIPG/2024/3552 (Griffen Small), and by the College of Science and Engineering at the University of Galway under the Millennium Fund scheme for the project "Modelling Brain Mechanics" (Valentina Balbi). Francesca Ballatore acknowledges support from the PNRR M4C2 through the project "Made in Italy Circolare e Sostenibile (MICS)", CUP: E13C22001900001. The authors are grateful to the anonymous reviewers for their constructive criticisms, helpful suggestions and insights.

References

1 S. Budday, T. C. Ovaert, G. A. Holzapfel, P. Steinmann and E. Kuhl, *Arch. Comput. Methods Eng.*, 2020, **27**, 1187–1230.
2 V. Balbi, A. Trotta, M. Destrade and A. N. Annaidh, *Soft Matter*, 2019, **15**, 5147–5153.
3 M. Destrade, M. D. Gilchrist, J. G. Murphy, B. Rashid and G. Saccomandi, *Int. J. Non Linear Mech.*, 2015, **75**, 54–58.
4 A. Greiner, N. Reiter, F. Paulsen, G. A. Holzapfel, P. Steinmann, E. Comellas and S. Budday, *Front. Mech. Eng.*, 2021, **7**, 708350.
5 B. Rashid, M. Destrade and M. D. Gilchrist, *J. Mech. Behav. Biomed. Mater.*, 2014, **33**, 43–54.
6 B. Rashid, M. Destrade and M. D. Gilchrist, *J. Mech. Behav. Biomed. Mater.*, 2013, **28**, 71–85.
7 B. Rashid, M. Destrade and M. D. Gilchrist, *Comput. Mater. Sci.*, 2012, **10**, 23–38.
8 S. Budday, G. Sommer, J. Haybaeck, P. Steinmann, G. A. Holzapfel and E. Kuhl, *Acta Biomater.*, 2017, **60**, 315–329.
9 W. Kang, L. Wang and Y. Fan, *J. Biomech.*, 2024, **162**, 111888.
10 C. Giverso and L. Preziosi, *Math. Med. Biol.*, 2010, **29**, 181–204.
11 D. Ambrosi and L. Preziosi, *Biomech. Model. Mechanobiol.*, 2009, **8**, 397–413.
12 C. Giverso and L. Preziosi, *Int. J. Non Linear Mech.*, 2013, **56**, 50–55.
13 H. Delingette and N. Ayache, *Handb. Numer. Anal.*, 2004, **12**, 453–550.
14 S. Ji, M. Ghajari, H. Mao, R. H. Kraft, M. Hajiaghamemar, M. B. Panzer, R. Willinger, M. D. Gilchrist, S. Kleiven and J. D. Stitzel, *Ann. Biomed. Eng.*, 2022, **50**, 1389–1408.
15 T. A. Connor, J. M. Clark, J. Jayamohan, M. Stewart, A. McGoldrick, C. Williams, B. M. Seemungal, R. Smith, R. Burek and M. D. Gilchrist, *Sports Med.*, 2019, **5**, 1–8.
16 A. Wineman, *Math. Mech. Solids*, 2009, **14**, 300–366.
17 C. S. Drapaca, S. Sivaloganathan and G. Tenti, *Math. Mech. Solids*, 2007, **12**, 475–501.
18 L. Anand and S. Govindjee, *Continuum Mechanics of Solids*, Oxford University Press, 2020.
19 R. M. Christensen, *Theory of Viscoelasticity: An Introduction*, Dover Publications, 2nd edn, 2003.
20 Y. C. Fung, *Biomechanics: Mechanical Properties of Living Tissues*, Springer Science & Business Media, 2nd edn, 1993.
21 R. De Pascalis, D. I. Abrahams and W. J. Parnell, *Proc. R. Soc. A*, 2014, **470**, 20140058.
22 T. Shearer, W. J. Parnell, B. Lynch, H. R. Screen and D. I. Abrahams, *J. Biomech. Eng.*, 2020, **142**, 071003.
23 S. Chatelin, A. Constantinesco and R. Willinger, *Biorheology*, 2010, **47**, 255–276.
24 S. E. Duenwald, R. Vanderby and R. S. Lakes, *Ann. Biomed. Eng.*, 2009, **37**, 1131–1140.
25 S. Nasseri, L. E. Bilston and N. Phan-Thien, *Rheol. Acta*, 2002, **41**, 180–192.
26 A. Karimi, M. Haghighatnama, A. Shojaei, M. Navidbakhsh, A. Motevalli Haghi and S. J. Adnani Sadati, *Proc. Inst. Mech. Eng., Part L*, 2016, **230**, 418–425.
27 C. Flynn, A. J. Taberner, P. M. F. Nielsen and S. Fels, *J. Mech. Behav. Biomed. Mater.*, 2013, **28**, 484–494.
28 D. B. MacManus, M. Maillet, S. O'Gorman, B. Pierrat, J. G. Murphy and M. D. Gilchrist, *J. Mech. Behav. Biomed. Mater.*, 2019, **99**, 240–246.
29 S. N. Sundaresh, J. D. Finan, B. S. Elkin, A. V. Basilio, G. M. McKhann and B. Morrison III, *Ann. Biomed. Eng.*, 2022, **50**, 1452–1460.
30 S. N. Sundaresh, J. D. Finan, B. S. Elkin, C. Lee, J. Xiao and B. Morrison III, *Brain Multiphys.*, 2021, **2**, 100041.
31 D. B. MacManus, A. Menichetti, B. Depreitere, N. Famaey, J. Vander Sloten and M. Gilchrist, *Brain Multiphys.*, 2020, **1**, 100018.
32 M. Hosseini-Farid, A. Rezaei, A. Eslaminejad, M. Ramzanpour, M. Ziejewski and G. Karami, *Sci. Iran.*, 2019, **26**, 2047–2056.
33 D. Sahoo, C. Deck and R. Willinger, *J. Mech. Behav. Biomed. Mater.*, 2014, **33**, 24–42.
34 S. Chatelin, C. Deck and R. Willinger, *J. Biorheol.*, 2013, **27**, 26–37.
35 N. Daphalapurkar, J. Riglin, A. Mohan, J. Harris and J. Bernardin, *Int. J. Numer. Methods Biomed. Eng.*, 2023, **39**, e3744.
36 Z. H. Zhang, M. X. Pan, J. T. Cai, J. D. Weiland and K. Chen, *J. Biomed. Mater. Res., Part A*, 2018, **106**, 2151–2157.
37 A. Rycman, S. McLachlin and D. S. Cronin, *Front. Bioeng. Biotechnol.*, 2021, **9**, 693120.
38 J. Yu, N. Manouchehri, S. Yamamoto, B. K. Kwon and T. R. Oxland, *J. Mech. Behav. Biomed. Mater.*, 2020, **112**, 104044.
39 S. Jannesar, B. Nadler and C. J. Sparrey, *J. Biomech. Eng.*, 2016, **138**, 091004.
40 H. Helisaz, E. Belanger, P. Black, M. Bacca and M. Chiao, *Acta Biomater.*, 2024, **173**, 184–198.
41 H. Motallebzadeh, M. Charlebois and W. R. J. Funnell, *J. Acoust. Soc. Am.*, 2013, **134**, 4427–4434.
42 W. Yang, T. C. Fung, K. S. Chian and C. K. Chong, *J. Mech. Med. Biol.*, 2006, **6**, 261–272.
43 J. M. Huyghe, D. H. Van Campen, T. Arts and R. M. Heethaar, *J. Biomech.*, 1991, **24**, 841–849.

 This journal is © The Royal Society of Chemistry 2025

Open Access Article. Published on 23 May 2025. Downloaded on 6/19/2025 2:26:22 PM. This article is licensed under a Creative Commons Attribution 3.0 Unported Licence.

44 G. Criscenti, C. De Maria, E. Sebastiani, M. Tei, G. Placella, A. Speziali, G. Vozzi and G. Cerulli, *J. Biomech.*, 2015, **48**, 4297–4302.
45 S. D. Abramowitch and S. L. Woo, *J. Biomed. Eng.*, 2004, **126**, 92–97.
46 J. R. Funk, G. W. Hall, J. R. Crandall and W. D. Pilkey, *J. Biomech. Eng.*, 2000, **122**, 15–22.
47 I. Bah, N. R. J. Fernandes, R. L. Chimenti, J. Ketz, A. S. Flemister and M. R. Buckley, *J. Mech. Behav. Biomed. Mater.*, 2020, **112**, 104031.
48 R. Springhetti and N. S. Selyutina, *Meccanica*, 2018, **53**, 519–530.
49 N. S. Selyutina, I. I. Argatov and G. S. Mishuris, *Mech. Res. Commun.*, 2015, **67**, 24–30.
50 A. Giudici, K. W. F. van der Laan, M. M. van der Bruggen, S. Parikh, E. Berends, S. Foulquier, T. Delhaas, K. D. Reesink and B. Spronck, *Biomech. Model. Mechanobiol.*, 2023, **22**, 1607–1623.
51 F. Dadgar-Rad and N. Firouzi, *Int. J. Appl. Mech.*, 2021, **13**, 2150036.
52 R. De Pascalis, D. I. Abrahams and W. J. Parnell, *Int. J. Eng. Sci.*, 2015, **88**, 64–72.
53 M. Righi and V. Balbi, *Modeling Biomaterials*, Springer, 2021, ch. 3, pp. 71–103.
54 V. Balbi, T. Shearer and W. J. Parnell, *Math. Mech. Solids*, 2023, 1–25.
55 V. Balbi, T. Shearer and W. J. Parnell, *Proc. R. Soc. A*, 2018, **474**, 20180231.
56 R. De Pascalis, W. J. Parnell, D. I. Abrahams, T. Shearer, D. M. Daly and D. Grundy, *Proc. R. Soc. A*, 2018, **474**, 20180102.
57 D. B. MacManus, B. Pierrat, J. G. Murphy and M. D. Gilchrist, *Sci. Rep.*, 2017, **7**, 13729.
58 A. Menichetti, D. B. MacManus, M. D. Gilchrist, B. Depreitere, J. Vander Sloten and N. Famaey, *Int. J. Eng. Sci.*, 2020, **155**, 103355.
59 A. Garo, M. Hrapko, J. A. W. Van Dommelen and G. W. M. Peters, *Biorheology*, 2007, **44**, 51–58.
60 B. Rashid, M. Destrade and M. D. Gilchrist, *J. Mech. Behav. Biomed. Mater.*, 2012, **14**, 113–118.
61 B. Rashid, M. Destrade and M. D. Gilchrist, *J. Biomech.*, 2013, **46**, 1276–1281.
62 K. B. Arbogast and S. S. Margulies, *J. Biomech.*, 1998, **31**, 801–807.
63 B. Rashid, M. Destrade and M. D. Gilchrist, *Comput. Mater. Sci.*, 2012, **64**, 295–300.
64 M. Destrade, Y. Du, J. Blackwell, N. Colgan and V. Balbi, *Phys. Rev. E*, 2023, **107**, L053001.
65 British Standards, Physical Testing of Rubber, British Standards Institution Technical Report BS 903-0:2012, 2012.
66 S. Yan, D. Jia, Y. Yu, L. Wang, Y. Qiu and Q. Wan, *Eur. J. Mech. A/Solids*, 2021, **86**, 104154.
67 R. S. Rivlin, *Philos. Trans. R. Soc. London, Ser. A*, 1949, **242**, 173–195.
68 J. H. Poynting, *Proc. R. Soc. London, Ser. A*, 1909, **82**, 546–559.
69 S. P. A. Narayan, J. M. Krishnan, A. P. Deshpande and K. R. Rajagopal, *Mech. Res. Commun.*, 2012, **43**, 66–74.
70 The MathWorks Inc., Documentation for sgolayfilt, **https://mathworks.com/help/signal/ref/sgolayfilt.html**.
71 P. Ciarletta and M. Destrade, *IMA J. Appl. Math.*, 2014, **79**, 804–819.
72 M. Mooney, *J. Appl. Phys.*, 1940, **11**, 582–592.
73 R. S. Rivlin, *Philos. Trans. R. Soc. London, Ser. A*, 1948, **241**, 379–397.
74 G. A. Holzapfel, *Nonlinear Solid Mechanics: A Continuum Approach for Engineering*, John Wiley & Sons Ltd., 2000.
75 R. W. Ogden, *Non-Linear Elastic Deformations*, Dover Publications, 1997.
76 O. Morrison, M. Destrade and B. B. Tripathi, *Acta Biomater.*, 2023, **169**, 66–87.
77 K. M. Labus and C. M. Puttlitz, *J. Mech. Phys. Solids*, 2016, **96**, 591–604.
78 S. Budday, R. Nay, R. De Rooij, P. Steinmann, T. Wyrobek, T. C. Ovaert and E. Kuhl, *J. Mech. Behav. Biomed. Mater.*, 2015, **46**, 318–330.
79 M. D. Gilchrist, B. Rashid, J. G. Murphy and G. Saccomandi, *Math. Mech. Solids*, 2013, **18**, 622–633.
80 The MathWorks Inc., *Documentation for fmincon*, **https://mathworks.com/help/optim/ug/fmincon.html**.
81 A. Anssari-Benam, M. Destrade and G. Saccomandi, *Philos. Trans. R. Soc., A*, 2022, **380**, 20210325.
82 M. Destrade, G. Saccomandi and I. Sgura, *Proc. R. Soc. A*, 2017, **473**, 20160811.
83 M. Alnæs, J. Blechta, J. Hake, A. Johansson, B. Kehlet, A. Logg, C. Richardson, J. Ring, M. E. Rognes and G. N. Wells, *Arch. Numer. Software*, 2015, **3**, 9–23.
84 A. Logg, K. A. Mardal and G. Wells, *Automated Solution of Differential Equations by the Finite Element Method*, Springer, 2012.
85 U. Ayachit, *The ParaView Guide: A Parallel Visualization Application*, Kitware Inc., 2015.
86 R Core Team, *Documentation for TukeyHSD*, **https://www.rdocumentation.org/packages/stats/versions/3.6.2/topics/TukeyHSD**.
87 D. B. MacManus and M. Ghajari, *Brain Multiphys.*, 2022, **3**, 100059.
88 A. Tamura, S. Hayashi, I. Watanabe, K. Nagayama and T. Matsumoto, *J. Biomech. Sci. Eng.*, 2007, **2**, 115–126.
89 D. Sahoo, C. Deck and R. Willinger, *Accid. Anal. Prev.*, 2016, **92**, 53–70.
90 W. G. Knauss and J. Zhao, *Mech. Time-Depend. Mater.*, 2007, **11**, 199–216.
91 J. N. Antonakakis, P. Bhargava, K. C. Chuang and A. T. Zehnder, *J. Appl. Polym. Sci.*, 2006, **100**, 3255–3263.
92 J. Ciambella, A. Paolone and S. Vidoli, *Mech. Mater.*, 2010, **42**, 932–944.
93 E. G. Takhounts, J. R. Crandall and K. Darvish, *Stapp Car Crash J.*, 2003, **47**, 107–134.
94 L. E. Bilston, Z. Liu and N. Phan-Thien, *Biorheology*, 2001, **38**, 335–345.
95 R. Lilley, A. Reynaud, P. D. Docherty, N. Smith and N. Kabaliuk, *IFAC-Papers Online*, 2020, **53**, 16275–16280.

96 Y. Feng, R. J. Okamoto, R. Namani, G. M. Genin and P. V. Bayly, *J. Mech. Behav. Biomed. Mater.*, 2013, **23**, 117–132.
97 A. Banstola and J. N. J. Reynolds, *Front. Vet. Sci.*, 2022, **9**, 961413.
98 W. Lee, S. D. Lee, M. Y. Park, L. Foley, E. Purcell-Estabrook, H. Kim and S. S. Yoo, *BMC Vet. Res.*, 2015, **11**, 1–8.
99 T. J. Horgan and M. D. Gilchrist, *Int. J. Crashworthiness*, 2003, **8**, 353–366.

Open Access Article. Published on 23 May 2025. Downloaded on 6/19/2025 2:26:22 PM.
This article is licensed under a Creative Commons Attribution 3.0 Unported Licence.